algorithms

MDPI

Article

Collision of an Obstacle by an Elastic Bar in a Gravity Field: Solution with Discontinuous Velocity and Space-Time Primal-Dual Active Set Algorithm

Victor A. Kovtunenko [1,2]

[1] Department of Mathematics and Scientific Computing, Karl-Franzens University of Graz, NAWI Graz, Heinrichstr. 36, 8010 Graz, Austria; victor.kovtunenko@uni-graz.at
[2] Siberian Division of the Russian Academy of Sciences, Lavrentyev Institute of Hydrodynamics, Novosibirsk 630090, Russia

Abstract

A class of one-dimensional dynamic impact models is investigated with respect to non-smooth velocities using variational inequalities and space-time finite element approximation. For the problem of collision of a rigid obstacle by an elastic bar in the gravitational field, a benchmark based on particular solutions to the wave equation is constructed on a partition of rectangle domains. The full discretization of the collision problem is carried out over a uniform space-time triangulation and extended to distorted meshes. For the solution of the corresponding variational inequality, a semi-smooth Newton-based primal-dual active set algorithm is applied. Numerical experiments demonstrate advantages over time-step approximation: a high-precision numerical solution is computed in a few iterations without any spurious oscillations.

Keywords: impact contact dynamics; variational inequality; discontinuous velocity; space-time finite element; primal-dual active set

Academic Editor: Nargiz Sultanova

Received: 16 December 2025
Revised: 9 January 2026
Accepted: 14 January 2026
Published: 20 January 2026

1. Introduction

We study a class of dynamic contact and impact models with discontinuous velocities, whose motion is described by the one-dimensional (1D) wave equation. The space-time (ST) finite-element (FE) approximation provides us with a weak solution to evolutionary problems in a variational setting [1–3]. For benchmarking, the collision of a rigid obstacle by an initially undeformed elastic bar moving with an initial speed is considered in a gravity field. A benchmark solution before rebound is constructed analytically along characteristics of the wave equation, comprising piecewise quadratic functions. Approximate iterative solutions after rebound are computed by the use of a space-time primal-dual active set (PDAS) algorithm stemming from semi-smooth Newton (SSN) methods [4–6]. For implementation issues of the PDAS for contact dynamic models, we cite [7–9].

The general context of stationary and dynamic modeling in contact mechanics can be found in [10–12]. We refer to the existence of solutions to hyperbolic variational inequalities established in [13–15], in particular, to the boundary obstacle problem for a wave equation considered in [16–19]. Relevant results for parabolic variational inequalities are given in [20–22]. We cite optimization-based methods for evolutionary models [23–26], their controllability [27,28], asymptotic analysis [29–31] and regularization framework [32–34]. The variational theory of constrained optimization problems describing non-smooth contact of elastic bodies, in particular non-penetrating cracks, was developed in [35–37] and other

works. Within the broader context of nonlinear dynamic modeling and vibration control in complex mechanical systems, we mention some relationships between impact noise and vibration acoustics, e.g., see the real-world application to underwater vehicles in [38].

For the Galerkin method and FE approximation of time-dependent problems, we refer the readers to [39–41], in particular, to the 1D linear elastodynamic problem with unilateral constraints [42]. Assuming smooth velocities, there was developed a Hilber–Hughes–Taylor α-method, which generalizes the Newmark family of time-stepping schemes; see [43–45]. Within the theory of measure differential inclusions, a time-stepping concept is elaborated when a discontinuous velocity is multiplied by the restitution coefficient. In this way, the dynamic of an impacting bar was treated numerically in [46] in accordance with experimental studies from [47].

In contact dynamics, even well-established time-stepping methods meet principal difficulties encountering instability. On the one hand, a solution may start to oscillate in contact nodes and rapidly collapse by decreasing step size. On the other hand, when spurious oscillations are suppressed by damping, mechanical energy may become dissipative in time. For remedy, in [48–50] we suggested a new method of space-time approximation accounting for non-smooth velocities, which is based on the PDAS iterative algorithm over uniform ST-triangulations. The ST-PDAS solution is of high precision and free of spurious oscillations, whereas the energy is non-dissipative.

For the benchmarks, in [48–50], there were derived in the closed form non-smooth solutions to a 1D wave equation constrained by a boundary obstacle under different initial and boundary data. Avoiding damping and conservative forces, the analytical solution in the space-time domain was given by piecewise linear functions comprised along characteristics of the wave equation within arbitrary times. In the current contribution, we adapt the ST-PDAS algorithm for treatment of the 1D wave equation in a gravity field. In this case, a nonlinear solution can comprise piecewise quadratic functions on a partition of the space-time domain within some proper time bound. The non-linearity challenges obtaining novel theoretical and numerical results. Namely, the main new elements are the inclusion of a constant gravity force, the construction of a non-smooth analytical benchmark solution (see Theorem 1), and the associated numerical tests. In the presence of gravity, we can express the solution to the collision problem in the closed form only prior to rebound.

To gain insight into the principal difficulty here, we consider an example model in one variable describing the motion of a point mass with the gravity $-g < 0$ starting at $t = 0$ at the deep $x = -H < 0$; see the illustration in the left plot of Figure 1. After scaling by mass, we will consider the unit of g to be velocity over time. Initiated by the speed $v_0 > 0$, the mass moves in time $t > 0$ upwards along the trajectory $x = -H + v_0 t - gt^2/2$ until colliding with the obstacle $x = 0$ at the time $\tau > 0$ that solves the quadratic equation

$$-H + v_0 \tau - \frac{g}{2}\tau^2 = 0. \tag{1}$$

The collision time justifying (1) is calculated as follows:

$$\tau = \frac{v_0 - \sqrt{v_0^2 - 2gH}}{g} = \frac{2H}{v_0 + \sqrt{v_0^2 - 2gH}} \quad \text{for } v_0 \geq \sqrt{2gH}. \tag{2}$$

The trajectory $x = u(t)$ can be described by the following nonlinear Cauchy problem:

$$\begin{cases} u_{tt}(t) = -\lambda(t) - g, \quad 0 \geq u(t) \perp \lambda(t) \leq 0 \quad \text{for } t > 0, \\ u(0) = -H, \quad u_t(0) = v_0. \end{cases} \tag{3}$$

Here we use the subscript t on a variable, which is common shorthand for the time derivative, and the subscript tt for the second time derivative. The contact conditions in (3) are given in the complementarity form, where λ implies a non-tensile contact force. The problem allows multiple solutions after collision,

$$\begin{cases} u(t) = (t-\tau)\big(v_0 - \frac{g}{2}(t+\tau)\big), \quad \lambda(t) = 0 & \text{for } t \in [0,\tau), \\ u(t) = 0, \quad \lambda(t) = -g & \text{for } t \in [\tau, r), \\ u(t) = (r-t)\big(v_1 - \frac{g}{2}(r-t)\big), \quad \lambda(t) = 0 & \text{for } t \geq r, \end{cases} \tag{4}$$

with an arbitrary rebound velocity $v_1 \geq 0$ at an arbitrary rebound time $r \geq \tau$. In the derivation of expression (4) we have used the identity (1). The solution is non-smooth, obeying discontinuous velocity and distributional acceleration. A non-unique trajectory $x = u(t)$ is drawn in the right plot of Figure 1. We extend the point-mass model to an elastic 1D bar. We construct a solution analytically before rebound starts and use it as a benchmark for computer simulation. After rebound, a numerical solution is computed.

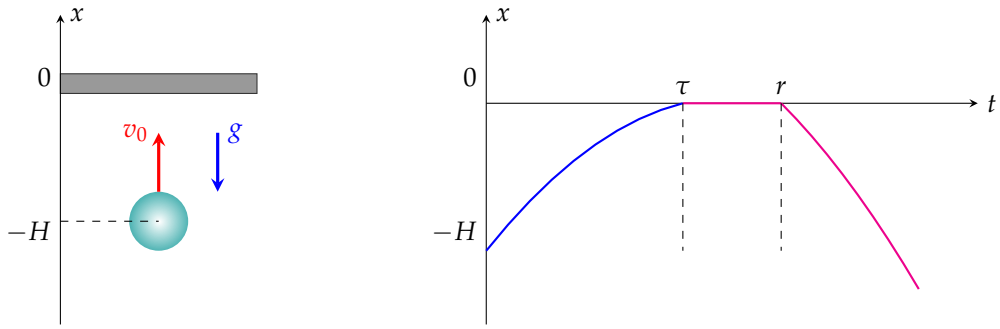

Figure 1. Collision of obstacle by mass in a gravity field (**left**); a trajectory $x = u(t)$ (**right**).

The structure of the paper is the following: The dynamic contact problem for an initially undeformed elastic bar, which moves with an initial speed in the gravitational field and collides with a rigid half-space obstacle, is formulated in Section 2. The primal-dual variational formulation of the collision problem is introduced in a 2D space-time rectangle. We construct analytically its weak solution, allowing discontinuous velocity and mechanical strain on a partition along characteristics of the equation of motion before rebound. This provides us with a benchmark for computer simulations implemented by piecewise linear FEM over uniform ST-triangulation in Section 3. We adapt an ST-PDAS algorithm for iteration of the complementarity conditions. In Section 4, the displacement field on the contact boundary and mechanical energy are examined with respect to the numerical error under decreasing step size. From our experiments we conclude that the ST-PDAS solution is of high precision and free of spurious oscillations. In Section 5, a globalization strategy based on the use of finite differences is suggested for distorted meshes to preserve the contact force balance.

2. Weak Solution to Collision Problem in Gravity Field

We consider a uniform linear elastic bar of length $L > 0$, unit mass and rigidity, which allows either tension or compression strain. Let the bar in its undeformed state occupy the space interval $x \in [-H - L, -H]$ posed vertically at the deep $-H < 0$ below the origin. It starts motion upwards with the prescribed initial speed $v_0 > 0$ at $t = 0$ under the gravity $-g < 0$ scaled by mass; see the illustration in Figure 2.

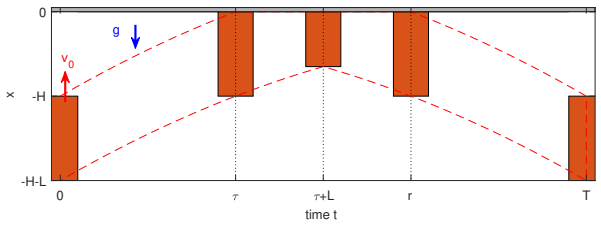

Figure 2. Collision of obstacle at $x = 0$ by elastic bar moving with initial speed v_0 in gravity field g.

In the ST-rectangle $Q := (0,T) \times (0,L)$ with the boundary ∂Q and some final time $T > 0$, the bar displacement $u(t,x)$ is described by the wave equation

$$u_{tt}(t,x) - u_{xx}(t,x) = -g \quad \text{for } (t,x) \in Q, \tag{5}$$

and supported by initial conditions at $t = 0$,

$$u(0,x) = -H, \quad u_t(0,x) = v_0 \quad \text{for } x \in (0,L). \tag{6}$$

Here and thereafter, the subscripts with respect to t and x stand for partial derivatives. When $t = 0$ and $x \in (0,L)$, the position of the elastic bar is $x - L + u(0,x) \in (-H-L, -H)$. We assume that the bar is free at one end, $x = 0$, which is described by zero strain,

$$u_x(t,0) = 0 \quad \text{for } t \in (0,T), \tag{7}$$

and it collides with the rigid obstacle at the other end $x = L$. The non-penetration is described by complementarity conditions at the contact boundary $\Gamma := \{t \in (0,T),\ x = L\}$,

$$0 \geq u(t,L) \perp \lambda(t) \leq 0 \quad \text{for } t \in (0,T). \tag{8}$$

In (8), λ stands for the normal contact force, which in case of smooth functions equals the normal reaction

$$\lambda(t) = u_x(t,L) \quad \text{for } t \in (0,T). \tag{9}$$

Next we derive a variational formulation to the boundary value problem (Equations (5)–(9)).

For smooth functions u, v in the closure $\overline{Q} := Q \cup \partial Q$, the following Green formula holds

$$\int_Q (u_{tt} - u_{xx}) v \, dxdt = \int_Q (-u_t v_t + u_x v_x) \, dxdt + \int_0^L u_t v \, dx\Big|_{t=0}^T - \int_0^T u_x v \, dt\Big|_{x=0}^L.$$

Multiplying the wave Equation (5) with a smooth function $v(t,x)$ in $\overline{Q}$ and integrating by parts over Q, with the help of Green's formula and conditions (Equations (6), (7) and (9)) we get

$$-\int_Q gv \, dxdt = \int_Q (-u_t v_t + u_x v_x) \, dxdt - \int_0^L v_0 v\big|_{t=0} \, dx - \int_0^T \lambda v\big|_{x=L} \, dt \tag{10}$$

for test functions such that

$$v(T,x) = 0 \quad \text{for } x \in (0,L). \tag{11}$$

Conditions prescribed either at initial time by Equation (6) or at final time by Equation (11) distinguish the linear sub-spaces,

$$H^1_{0*}(0,T) := \{v \in H^1(0,T),\ v(0) = 0\}, \quad H^1_{*0}(0,T) := \{v \in H^1(0,T),\ v(T) = 0\}.$$

Within the Petrov–Galerkin concept, we look for a weak solution in the trial space,

$$V_{0*} := L^2(0,T;H^1(0,L)) \cap H^1_{0*}(0,T;L^2(0,L)),$$

justifying Equation (10) for functions v from the test space,

$$V_{*0} := L^2(0,T;H^1(0,L)) \cap H^1_{*0}(0,T;L^2(0,L)).$$

Namely, we find the pair $(u+H,\lambda) \in V_{0*} \times L^2(0,T)$ such that

$$\begin{cases} u(t,L) \le 0, \quad \lambda(t) \le 0 \quad \text{for } t \in (0,T), \quad \displaystyle\int_0^T \lambda u\big|_{x=L}\, dt = 0, \\ \displaystyle\int_Q (-u_t v_t + u_x v_x + gv)\, dxdt - \int_0^L v_0 v\big|_{t=0}\, dx = \int_0^T \lambda v\big|_{x=L}\, dt \end{cases} \tag{12}$$

for all test functions $v \in V_{*0}$. In the case of a smooth solution $u \in H^2(Q)$, variational Equation (12) follows that Equations (5)–(9) hold pointwise.

It is worth noting that, if variational smoothness $u \in H^1(0,L)$ holds only, then strain u_x on the contact boundary at $x = L$ associated in Equation (9) to λ is determined generally as the $H^{-1/2}$-distribution. In this case, reducing λ from the primal-dual formulation (Equation (12)), we can relax it to the variational inequality. Find $u + H \in V_{0*}$ such that

$$\begin{cases} u(t,L) \le 0 \quad \text{for } t \in (0,T), \\ \displaystyle\int_Q \big(-u_t(v_t - u_t) + u_x(v_x - u_x) + g(v-u)\big)\, dxdt - \int_0^L v_0(v\big|_{t=0} + H)\, dx \ge 0 \\ \text{for all } v - u \in V_{*0} \text{ such that } v(t,L) \le 0 \text{ for } t \in (0,T). \end{cases} \tag{13}$$

The contact force λ can be recovered from Equation (10). For $T \le \tau + L$ before rebound starts, we construct a weak solution to the boundary value problem (Equations (5)–(9)), hence to variational problems (Equations (12) and (13)), in the closed form.

Theorem 1. *For the collision time τ determined in Equations (1) and (2) and the final time $T = \tau + L$, let the gravitational force g and initial speed v_0 satisfy the bilateral bounds*

$$gL \le v_0 - g\tau \le 1. \tag{14}$$

On the partition of the rectangle $\overline{Q} = I \cup A$ along straight-line characteristics into two sets,

$$\begin{cases} I := \{(t,x) \in \overline{Q} : \ x - L \le \tau - t\}, \\ A := \{(t,x) \in \overline{Q} : \ x - L \ge \tau - t\}, \end{cases} \tag{15}$$

solution to the collision problem (Equations (5)–(9)) is given by explicit formula

$$u(t,x) = \begin{cases} (t-\tau)\big(v_0 - \frac{g}{2}(t+\tau)\big) & \text{in } I, \\ (L-x)\big(v_0 - gt + \frac{g}{2}(L-x)\big) & \text{in } A, \end{cases} \tag{16}$$

with the contact force on the contact boundary,

$$\lambda(t) = \begin{cases} 0 & \text{on } \Gamma \cap I, \\ -v_0 + gt & \text{on } \Gamma \cap A. \end{cases} \tag{17}$$

Moreover, it not penetrates the obstacle over all space-time points,

$$u \le L - x \quad \text{for } (t,x) \in \overline{Q} \tag{18}$$

The mechanical energy of the bar defined by the time-dependent integral formula

$$E(t) := \frac{1}{2}\int_0^L (u_t^2 + u_x^2)\,dx \quad \textit{for } t \in [0, T] \tag{19}$$

is comprised by the following functions:

$$E(t) = \begin{cases} \frac{1}{2}L(v_0 - gt)^2 & \textit{for } t \in [0, \tau), \\ \frac{1}{2}L(v_0 - gt)^2 + \frac{1}{2}g(v_0 - gt)(t-\tau)^2 + \frac{1}{3}g^2(t-\tau)^3 & \textit{for } t \in [\tau, \tau + L]. \end{cases} \tag{20}$$

For convenience, the partition in Equation (15) is drawn in Figure 3.

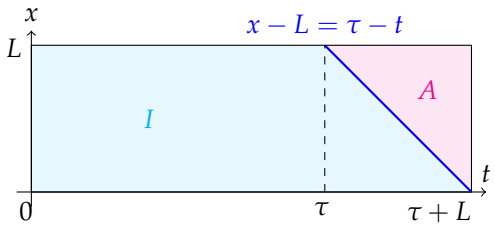

Figure 3. Partition of the rectangle Q with $T = \tau + L$ into sets I and A.

Before starting a proof, we give a physical interpretation to the bilateral bounds in Equation (14). In virtue of Equation (2), $v_0 - g\tau = \sqrt{v_0^2 - 2gH} \geq 0$. From one side, if $v_0 - g\tau < gL$, then the initial speed v_0 is too low for the elastic wave to reach the endpoint $x = 0$ at $t = \tau + L$ before the bar starts leaving contact. On the other side, the upper threshold prevents too high initial speeds $v_0 - g\tau > 1$ such that the full bar would be compressed into a point (that is, $u(t, \cdot) = L - x$ in Equation (18)) at some time $t \in (\tau, \tau + L)$.

Proof. The composition defined in Equations (16) and (17) fulfills the following:

$$\begin{cases} u_t = v_0 - gt, \quad u_x = 0, \quad u_{tt} = -g, \quad u_{xx} = 0 & \text{in } I; \\ u = -H,\ u_t = v_0 \text{ as } t = 0, \quad u_x = 0 \text{ as } x = 0, L & \text{on } \partial I; \\ u = (t-\tau)\big(v_0 - \frac{g}{2}(t+\tau)\big), \quad u_t - u_x = v_0 - gt & \text{on } I \cap A; \\ u_t = -g(L-x), \quad u_x = -v_0 + g(t - L + x), \quad u_{tt} = 0, \quad u_{xx} = g & \text{in } A; \\ u = 0,\ u_x = -v_0 + gt \text{ as } x = L, \quad u_x = 0 \text{ as } x = 0 & \text{on } \partial A. \end{cases} \tag{21}$$

It comprises a continuous piecewise quadratic function with the continuous normal derivative $u_t - u_x$ across the interface $I \cap A$ having the normal $(1, 1)/\sqrt{2}$. This function satisfies the wave Equation (5), initial Equation (6) and boundary Equations (7) and (9).

We check the non-penetration condition (Equation (18)) and inequalities in Equation (8). The tensile contact force in Equation (9) needs

$$u_x(t, L) = -v_0 + gt \leq 0 \quad \text{for } t \in (\tau, \tau + L). \tag{22}$$

The linear function suffices to justify Equation (22) at the end points, that is,

$$-v_0 + g\tau \leq 0, \quad -v_0 + g(\tau + L) \leq 0,$$

which is assumed within Equation (14). For all $L - x \geq 0$ and $t \leq \tau$ in I, from Equation (16) we estimate

$$u = (t-\tau)\big(v_0 - g\tau - \frac{g}{2}(t-\tau)\big) \leq (t-\tau)(v_0 - g\tau) \leq L - x \quad \text{for } t \in (0, \tau), \tag{23}$$

since it holds according to Equation (2),

$$0 \le v_0 - g\tau = \sqrt{v_0^2 - 2gH}.$$

For $t \ge \tau$ in I, the fulfillment of upper bound,

$$u = (t-\tau)\big(v_0 - \frac{g}{2}(t+\tau)\big) \le L - x \quad \text{for } t - \tau \le L - x \tag{24}$$

at the end points $t = \tau$ and $t = \tau + L$,

$$0 \le v_0 - g\tau \le 1, \quad 0 \le v_0 - g\tau - \frac{g}{2}L \le 1,$$

is guaranteed by Equation (14). Similarly, for $t \ge \tau$ in A, we estimate the linear term

$$u = (L-x)\big(v_0 - gt + \frac{g}{2}(L-x)\big) \le L - x \quad \text{for } t - \tau \ge L - x \tag{25}$$

at the end points $(t,x) = (\tau, L)$ and $(t,x) = (\tau + L, 0)$:

$$0 \le v_0 - g\tau \le 1, \quad 0 \le v_0 - g\tau - \frac{g}{2}L \le 1,$$

which holds true in virtue of Equation (14). Equations (23)–(25) verify together the non-penetration condition (Equation (18)) holding over the whole rectangle $\overline{Q}$, in particular, at the contact boundary Γ within the complementarity conditions (Equation (8)).

Let us denote for brevity the jumps of u over two faces of the interface,

$$[\![u]\!] = u\big|_{\partial A \cap I} - u\big|_{\partial I \cap A}.$$

Green's formula for piecewise-smooth functions u, v on the partition $\overline{Q} = I \cup A$ gives

$$\int_{I\cup A} (u_{tt} - u_{xx}) v \, dtdx = \int_{I\cup A} (-u_t v_t + u_x v_x) \, dtdx$$
$$- \int_{I\cap A} \frac{1}{\sqrt{2}} [\![(u_t - u_x)v]\!] \, dS + \int_0^L u_t v \, dx\big|_{t=0}^T - \int_0^T u_x v \, dt\big|_{x=0}^L.$$

If $[\![v]\!] = 0$ such that $[\![(u_t - u_x)v]\!] = [\![u_t - u_x]\!]v$, then Equation (21) yields the variational equation for test functions $v \in V_{*0}$,

$$- \int_{I\cup A} gv \, dtdx = \int_{I\cup A} (-u_t v_t + u_x v_x) \, dtdx - \int_0^L v_0 v\big|_{t=0} dx - \int_0^T u_x v \, dt\big|_{x=L}. \tag{26}$$

It follows Equation (10) with $\lambda = u_x$ at $x = L$, and variational Equations (12) and (13).

Inserting Equation (21) into Equation (19), straightforward calculation leads to Equation (20) for the mechanical energy. The proof is completed. □

Further we will use the explicit Equations (14)–(20) from Theorem 1 for an analytical benchmark in computer simulation.

3. Full ST-FEM Discretiazation and ST-PDAS Algorithm

The full space-time discretization of the displacement u is realized over standard piecewise linear functions on uniform triangular meshes $\mathcal{T}_h$ building the FE-space,

$$V^h := \{v_h \in C^0(\overline{Q}),\ v_h|_K \in \mathbb{P}_1(K) \text{ for all } K \in \mathcal{T}_h,\ v_h(\cdot\,,0) = 0\}.$$

The respective trial and test function FE sub-spaces are

$$V^h_{0*} := \{v_h \in V^h,\ v_h(0,\cdot\,) = 0\}, \quad V^h_{*0} := \{v_h \in V^h,\ v_h(T,\cdot\,) = 0\}.$$

Let V^h be spanned by a set of hat-shaped basis functions $\{\phi_h\}$ associated with nodes $(t_h, x_h) \in \overline{Q}$ and supported in patches composed of adjacent triangles $K \in \mathcal{T}_h$ possessing the vertex (t_h, x_h). Next we discretize the contact force λ along the contact boundary Γ.

On Γ, the mesh $\mathcal{T}_h$ is represented by equidistant time points $t_m := hm$ for $m = 0, \dots, M$, with the time-step $h := T/M$ prescribed by integer M. These points build the partition $[0, T] = \bigcup_{m=1}^{M} \overline{T}_m$ into intervals $T_m := (t_{m-1}, t_m)$. Let the basis functions $\phi_0, \dots, \phi_M$ correspond to the boundary nodes $(t_0, L), \dots, (t_M, L)$, and other $\phi_h = 0$ on Γ. For discrete $u_h \in V^h$, we approximate its discontinuous gradient by the piecewise constant function $u_{hx}(\cdot\,, L)$ over T_m. Inserting in Equation (26) $u = u_h$ and $v = \phi_h \in V^h_{*0}$, we have

$$\int_Q (-u_{ht}\phi_{ht} + u_{hx}\phi_{hx} + g\phi_h)\,dxdt - \int_0^L v_0\phi_h|_{t=0}\,dx = \int_0^T u_{hx}\phi_h|_{x=L}\,dt. \tag{27}$$

For each of $\phi_h = \phi_m$ having the support on $(T_m \cup T_{m+1}) \cap \Gamma$ as $m = 0, \dots, M-1$, where $T_0 := \emptyset$, the integral over the contact boundary reads

$$\int_0^T u_{hx}\phi_m\,dt\big|_{x=L} = \frac{h}{2}\big(u_{hx}(\cdot\,, L)|_{T_m\cap\Gamma} + u_{hx}(\cdot\,, L)|_{T_{m+1}\cap\Gamma}\big)\phi_m|_{x=L}. \tag{28}$$

This determines the Lagrange multiplier $\lambda_h = (\lambda_1, \dots, \lambda_M)$ by piecewise constants

$$\lambda_m := u_{hx}(\cdot\,, L)|_{T_m\cap\Gamma}, \quad m = 1, \dots, M. \tag{29}$$

Using Equationss (27)–(29) we discretize the primal-dual variational problem (Equation (12)) as follows: Find $u_h + H \in V^h_{0*}$ and $\lambda_h \in \mathbb{R}^M$ such that for all basis functions $\phi_h \in V^h_{*0}$,

$$\begin{cases} u_h|_{T_m} \le 0, \quad \lambda_m \le 0, \quad m = 1, \dots, M, \quad \displaystyle\sum_{m=1}^{M} \lambda_m\big(u_h(t_{m-1}, L) + u_h(t_m, L)\big) = 0, \\ \displaystyle\int_Q (-u_{ht}\phi_{ht} + u_{hx}\phi_{hx} + g\phi_h)\,dxdt - \int_0^L v_0\phi_h|_{t=0}\,dx = \int_0^T \lambda_h\phi_h|_{x=L}\,dt. \end{cases} \tag{30}$$

Further we express Equation (30) in an algorithmic way.

It is useful to introduce the residuals on Γ:

$$r(\phi_m) := \int_Q (-u_{ht}\phi_{mt} + u_{hx}\phi_{mx} + g\phi_m)\,dxdt - \int_0^L v_0\phi_m\delta_{m0}\,dx, \quad m = 0, \dots, M-1, \tag{31}$$

which allow to calculate the Lagrange multiplier recurrently according to Equation (28),

$$\lambda_0 := 0, \quad \lambda_{m+1} = \frac{2}{h}r(\phi_m) - \lambda_m \quad \text{for } m = 0, \dots, M-1. \tag{32}$$

If $u_h(t_{m-1}, L)$ and $u_h(t_m, L)$ have the same sign on T_m for all m, then complementarity conditions in Equation (30) can be rewritten as nonlinear equations

$$\lambda_m = \min\big(0, \lambda_m - \frac{u_h(t_{m-1}, L) + u_h(t_m, L)}{2}\big), \quad m = 1, \dots, M. \tag{33}$$

In Equation (33), either $u_h(t, L) = 0$ for $t \in T_m \subset \mathcal{A}(u_h, \lambda_h)$, or $\lambda_m = 0$ for complementary $T_m \subset \mathcal{I}(u_h, \lambda_h)$, where we distinguish between active and inactive intervals T_m,

$$\begin{cases} \mathcal{A}(u_h, \lambda_h) := \{\cup T_m : \ \lambda_m - \dfrac{u_h(t_{m-1}, L) + u_h(t_m, L)}{2} < 0\}, \\ \mathcal{I}(u_h, \lambda_h) := \{\cup \overline{T}_m : \ \lambda_m - \dfrac{u_h(t_{m-1}, L) + u_h(t_m, L)}{2} \geq 0\}. \end{cases} \tag{34}$$

Using Equations (31)–(34), Equation (30) leads to the following implicit problem: Find $u_h + H \in V_{0*}^h$ and $\lambda_h \in \mathbb{R}^M$ such that

$$\begin{cases} u_h(t_{m-1}, L) + u_h(t_m, L) = 0 \text{ on } \mathcal{A}(u_h, \lambda_h), \quad \lambda_m = 0 \text{ on } \mathcal{I}(u_h, \lambda_h), \\ \lambda_{m+1} = \dfrac{2}{h} r(\phi_m) - \lambda_m \quad \text{for } m = 0, \ldots, M-1, \quad r(\phi_h) = 0 \text{ for } \phi_h|_\Gamma = 0, \\ \displaystyle\int_Q (-u_{ht}\phi_{ht} + u_{hx}\phi_{hx} + g\phi_h)\, dxdt - \int_0^L v_0 \phi_h|_{t=0}\, dx = r(\phi_h) \end{cases} \tag{35}$$

for all basis functions $\phi_h \in V_{*0}^h$. The primal-dual active set algorithm iterates Equation (35) over active sets (Equation (34)).

Based on our experiments, we support the initialization and iteration steps of Algorithm 1 by the following implementation hints.

1a. Final time extension: Since basis functions $\phi_1, \ldots, \phi_M$ in the trial space V_{0*}^h differ from basis functions $\phi_0, \ldots, \phi_{M-1}$ in the test space V_{*0}^h, it is useful to extend the computational domain by two fictitious times t^{M+1}, t^{M+2}.

2a. Contact force balance: To keep the force balance in Equation (9), which might be violated, we implement finite differences at the time before collision $t^* = \tau - h$ and at the extension

$$\frac{u_h^k(t, L) - u_h^k(t, L-h)}{h} = 0 \quad \text{for } t = t^*, t^{M+1}, t^{M+2}. \tag{36}$$

Algorithm 1: (ST-PDAS.)

1. Initialization: Start with sets $\mathcal{A}^0 = \emptyset$ and $\mathcal{I}^0 = [0, T]$, set iteration number $k = 0$.

2. Iteration: Find $u_h^k + H \in V_{0*}^h$ such that $u_h^k = 0$ on $\mathcal{A}_h^k$ solving the linear equation:

$$\int_Q (-u_{ht}^k \phi_{ht} + u_{hx}^k \phi_{hx} + g\phi_h)\, dxdt - \int_0^L v_0 \phi_h|_{t=0}\, dx = 0 \tag{37}$$

for all basis functions $\phi_h \in V_{*0}^h$ with $\phi_h = 0$ on $\mathcal{A}_h^k$.

3. Complementary: Compute the residual $r_h^k \in \mathbb{R}^M$:

$$r^k(\phi_m) = \int_Q (-u_{ht}^k \phi_{mt} + u_{hx}^k \phi_{mx} + g\phi_m)\, dxdt - \int_0^L v_0 \phi_m \delta_{m0}\, dx \tag{38}$$

and recurse the Lagrange multiplier $\lambda_h^k \in \mathbb{R}^M$:

$$\lambda_0^k := 0, \quad \lambda_{m+1}^k = \frac{2}{h} r^k(\phi_m) - \lambda_m^k \quad \text{for } m = 0, \ldots, M-1. \tag{39}$$

4. Update: Reset active and inactive sets:

$$\begin{cases} \mathcal{A}^{k+1} = \{\cup T_m : \ \lambda_m^k - \dfrac{u_h^k(t_{m-1}, L) + u_h^k(t_m, L)}{2} < 0\}, \\ \mathcal{I}^{k+1} = \{\cup \overline{T}_m : \ \lambda_m^k - \dfrac{u_h^k(t_{m-1}, L) + u_h^k(t_m, L)}{2} \geq 0\}. \end{cases} \tag{40}$$

5. Termination: Exit if $\mathcal{A}^{k+1} = \mathcal{A}^k$ or cycling, else increase $k = k + 1$ and go to iteration step.

Further, we report on our computing tests of the ST-PDAS solution, and validate it for the analytical benchmark from Theorem 1.

4. Numerical Tests of Collision in Gravity Field

Let the parameters of the problems be the bar length $L = 1$, the initial depth $H = 1$, the final time $T = 6$, and the gravity $g = 0.01$. We set the initial speed $v_0 = H/2 + g = 0.51$, such that $\sqrt{v_0^2 - 2gH} = |H/2 - g| = 0.49$ yields the collision time $\tau = 2$ in Equation (2), and $v_0 - g\tau = \sqrt{v_0^2 - 2gH}$ satisfies the bilateral bounds (Equation (14)) in Theorem 1. The uniform ST-triangulation $\mathcal{T}_h$ of the rectangle $Q = (0,6) \times (0,1)$ is illustrated in Figure 4 in the left plot (a) in its undeformed state, and in the right plot (b) after deformation. Here, the mesh size $h = 6/M = 0.125$ yields $M + 1 = 49$ constrained points at the contact boundary Γ, and the number of degrees of freedom DOF $= (M+1)(M/6+1)$ =441 in $\overline{Q}$.

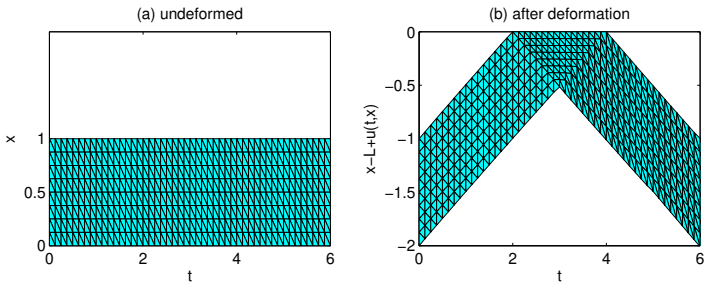

Figure 4. The uniform triangle mesh for $h = 0.125$ before deformation (**a**), and $x - L + u_h(t,x)$ after deformation (**b**).

We computed the collision problem in the primal-dual variational formulation (Equations (34) and (35)) iteratively using Algorithm 1. For $h = 0.125$, the history of displacement iterates $u_h^0(t_h, x_h)$, $u_h^1(t_h, x_h)$, and $u_h^2(t_h, x_h)$ over the rectangle is depicted in Figure 5. It is worth noting here that the small value prescribed for g reduces nonlinear phenomena; otherwise, large g may cause oscillation.

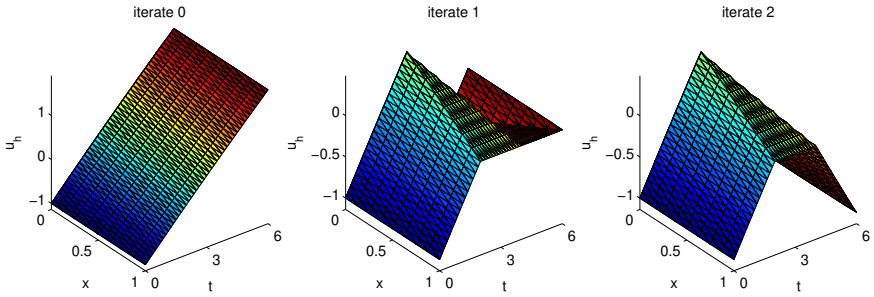

Figure 5. ST-PDAS iterates $k = 0, 1, 2$ of displacement $u_h^k(t_h, x_h)$ in $\overline{Q}$ for $h = 0.125$.

For all mesh sizes tested in the range $h = 0.02, \ldots, 0.5$, which corresponds to $M = 13, \ldots, 301$ constrained points, and the DOF $= 39, \ldots, 15964$, the algorithm terminated without cycling after three iteration steps. For the fine mesh as $h = 0.02$, the ST-PDAS iterates are presented in Figure 6 at $M = 301$ time points on the contact boundary as $x = 1$. There are depicted in the left plot (a): the three iterates of displacement $u_h^0(t_h, 1) \geq u_h^1(t_h, 1) \geq u_h^2(t_h, 1)$; in the center plot (b): the three iterates of Lagrange multiplier $\lambda_h^0(t_h) = 0$, $\lambda_h^1(t_h)$, $\lambda_h^2(t_h)$; and in the right plot (c): the iterates $k = 0, \ldots, 3$ of active set $\mathcal{A}_h^0 = \emptyset$, $\mathcal{A}_h^1 \supset \mathcal{A}_h^2 = \mathcal{A}_h^3$. In Figure 6 one can observe a typical for PDAS monotone behavior of displacements for $k \geq 0$ and active sets for $k \geq 1$, whereas there is no monotony for Lagrange multipliers.

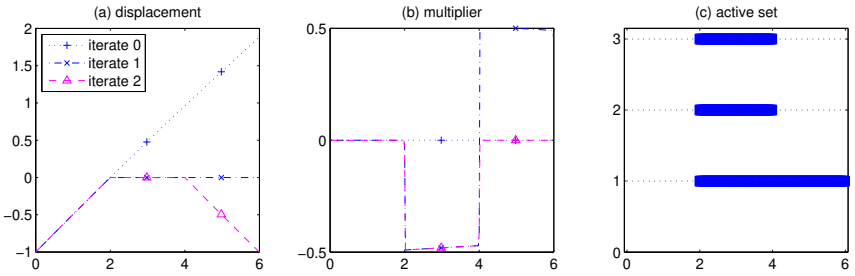

Figure 6. ST-PDAS iterates: displacement $u_h^k(t_h, 1)$ (**a**); multiplier $\lambda_h^k(t_h)$ (**b**); active set $\mathcal{A}_h^k$ (**c**).

To test the accuracy of the ST-PDAS solution, we compare it with the exact solution given in the rectangle $[0,3] \times [0,1]$ according to Equations (15)–(20). The numerical tests are computed for decreasing mesh sizes $h = 0.1, 0.05, 0.0\bar{3}, 0.025, 0.02$. In the left plot (a) of Figure 7 there are presented at the contact boundary Γ: the five curves of displacement $u_h(t_h, 1)$ at mesh nodes for $t_h \in [0,6]$, and the curve $u(t,1)$ for $t \in [0,3]$. Here one cannot visually distinguish between the curves even on coarse meshes. The right plot (b) draws the maximum over $t_h \in [0,3]$ of the absolute error $|u_h(t_h,1) - u(t_h,1)|$ versus decreasing h. The curve shows a linear convergence of numerical order 0.96 for displacements under the mesh refinement. The convergence rates are computed using least squares fit in the log-log plot. The linear rate matches a theoretical expectation for piecewise linear space-time elements.

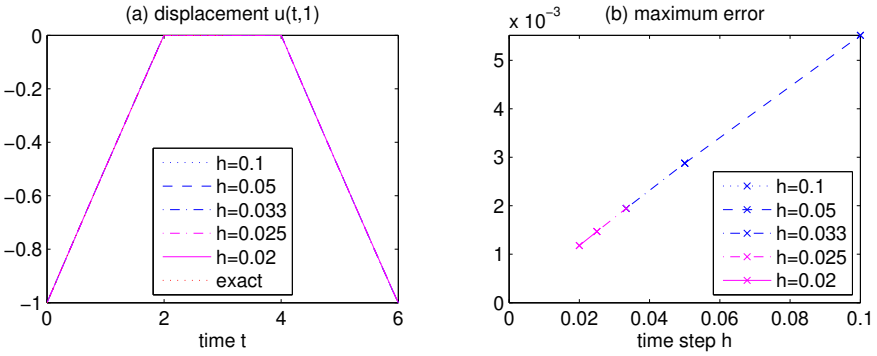

Figure 7. Discrete displacement $u_h(t_h, 1)$ (**a**), and absolute displacement error to exact solution $u(t,1)$ when step-size h decreases (**b**).

The discrete energy E_h is defined according to the integral formula

$$E_h(t) := \frac{1}{2} \int_0^L (u_{ht}^2 + u_{hx}^2)\, dx \quad \text{for } t \in [0,T] \tag{41}$$

for the FEM-solution $u_h(t, \cdot)$. The values $E_h(t_h)$ computed at $t_h \in [0,6]$ are depicted in the left plot (a) of Figure 8 together with the exact energy $E(t)$ given by analytical Equation (20) as $t \in [0,3]$. The five curves of discrete energy by varied mesh size h in the range $0.1, 0.05, 0.0\bar{3}, 0.025, 0.02$ show a discontinuous piecewise smooth behavior. No spurious oscillations are observed. The right plot (b) draws the maximum of the relative error $|E_h(t_h) - E(t_h)|/|E(t_h)| \cdot 100\%$ over $t_h \in [0,3]$, which is below 1.34%, and we observe a super-linear convergence rate of numerical order 1.45 for the energy approximation as h drops. The energy convergence rate corresponds to the square of the H^1-norm for a weak solution to the non-smooth problem.

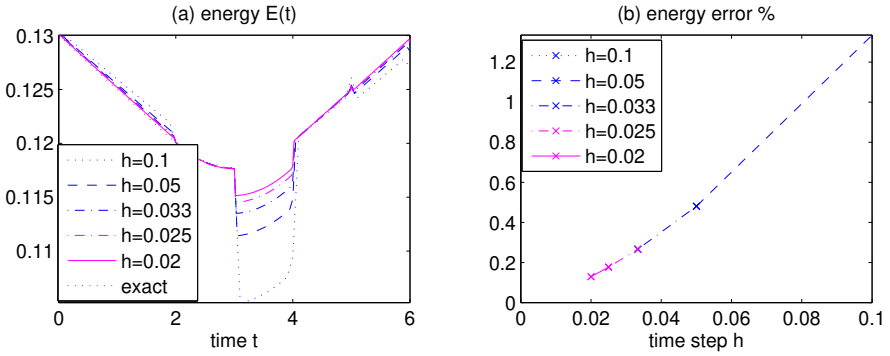

Figure 8. Discrete energy $E_h(t_h)$ (**a**), and relative energy error with respect to exact $E(t)$ when time step h decreases (**b**).

In the recent work [50], comparative benchmarks are presented for multiple impacts of a rigid obstacle by an initially deformed bar when neglecting gravity. The comparison with three of the most efficient methods in the literature is reported: the Nitsche-based Verlet time integration scheme proposed in [51], the restitution coefficient method from [46], and the mass redistribution method from [52]. Test cases highlight ST-FEM advantages in accuracy, iteration count, and energy conservation metrics. For relevant methods we refer also to the recently suggested Nitsche-based BEM-FEM coupling approach [53].

Finally, we validate the globalization strategy for the extension of the ST-FEM algorithm.

5. Globalization Strategy

We start with a cycling test case when the contact force balance is violated and the finite difference Equation (36) is dropped. The cycling is documented in Figure 9 depicting four iterates of displacement $u_h^k(t_h, 1)$, Lagrange multiplier $\lambda_h^k(t_h)$, and active set $\mathcal{A}_h^k$. In the right plot (c), one can observe that $\mathcal{A}_h^4 = \mathcal{A}_h^2$ happens; hence, the termination step of Algorithm 1 cannot be attained.

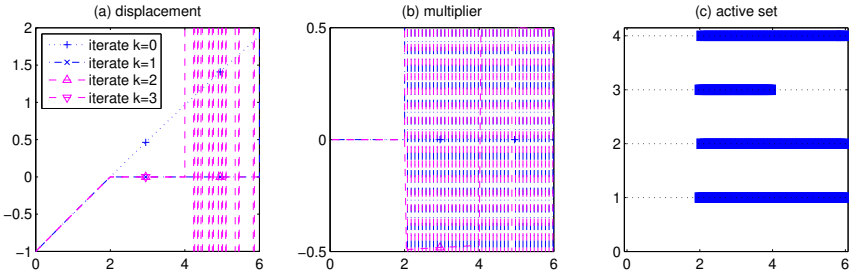

Figure 9. ST-PDAS cycling: displacement $u_h^k(t_h, 1)$ (**a**); multiplier $\lambda_h^k(t_h)$ (**b**); active set $\mathcal{A}_h^k$ (**c**).

Therefore, we will apply finite differences (Equation (36)) for all inactive nodes when extending numerical tests to distorted meshes. However, in this case we may lose accuracy of the discrete solution. The uniform triangle mesh as $h = 0.125$ drawn in the Figure 4a is distorted with random shifts in interior points $(t_h, x_h) \in Q$ within intervals $(-0.05h, 0.05h)$ in both the t and x directions. The distorted mesh is depicted in Figure 10a. Applying Algorithm 1 on this nonuniform mesh, iteration diverges as shown in the center plot (b) for the first four iterates. The iteration, implemented by the finite-difference Equation (36) on all nodes within inactive sets $\mathcal{I}^{k+1}$ in Equation (40), remedies the convergence after 4 iteration steps $\mathcal{A}_h^0 = \emptyset$, $\mathcal{A}_h^1 \supset \mathcal{A}_h^2 \supset \mathcal{A}_h^3 = \mathcal{A}_h^4$ as drawn in the Figure 10c.

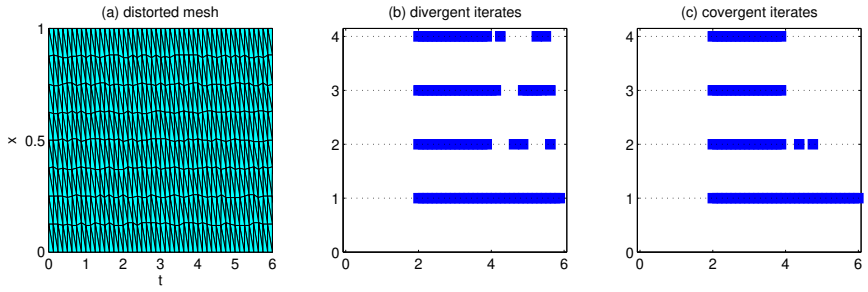

Figure 10. Distorted mesh (**a**); active set $\mathcal{A}_h^k$ for divergent iterates (**b**) and convergent iterates (**c**).

6. Conclusions

We develop a space-time primal-dual active set algorithm, stated in a primal-dual variational form, for the solution of nonlinear collision problems with non-smooth velocities accounting for a gravity g. The ST-PDAS solution is tested for the benchmark problem of a 1D elastic bar colliding with a rigid obstacle, which allows an analytical solution before rebound. Numerical tests validate convergence of the ST-PDAS iteration, as well as the high accuracy and non-dissipative behavior that is free of spurious oscillations under mesh refinement. A globalization strategy for further extension of numerical experiments is suggested based on preserving the contact force balance within inactive sets by using finite differences.

Compared to the previous works on the ST-PDAS algorithm, the main advantage concerns non-linearity phenomena. The closed-form solution stated in Theorem 1 is novel and merely extends classical d'Alembert methods with a gravitational term. It extends known prior works on longitudinal waves in bars and transverse waves in beams (see, e.g., [13]). However, analytical derivation in the presence of gravity is limited for postrebound dynamics. Extension of the analytical solution, when expressed by convergent series, to times after starting rebound could be the next task.

Whereas the algorithm aligns P1 finite elements for small g, increasing the gravity g may becomes approximation unstable. The discretization can be improved by the use of P2 polynomials in FE. The other issue concerns the fact that exceeding the bilateral bounds stated in Equation (14) for the problem data might lead to violation of the non-penetration condition (Equation (18)) inside the space-time rectangle. This needs further development of the ST-PDAS theory and computation.

Funding: This research received no external funding.

Data Availability Statement: Data is contained within the article.

Acknowledgments: V.A.K. acknowledges the support by the University of Graz.

Conflicts of Interest: The author declares no conflicts of interest.

References

1. Gangl, P.; Gobrial, M.; Steinbach, O. A space-time finite element method for the eddy current approximation of rotating electric machines. *Comput. Meth. Appl. Math.* **2025**, *25*, 441–457. [CrossRef]
2. Junker, P.; Wick, T. Space-time variational material modeling: A new paradigm demonstrated for thermo-mechanically coupled wave propagation. *Comput. Mech.* **2024**, *73*, 365–402. [CrossRef]
3. Steinbach, O.; Zank, M. Coercive space-time finite element methods for initial boundary value problems. *Electron. Trans. Numer. Anal.* **2020**, *52*, 154–194. [CrossRef]
4. Ito, K.; Kunisch, K. *Lagrange Multiplier Approach to Variational Problems and Applications*; SIAM: Philadelphia, PA, USA, 2008. [CrossRef]

5. Hintermüller, M.; Kovtunenko, V.A.; Kunisch, K. Generalized Newton methods for crack problems with non-penetration condition. *Numer. Meth. Partial Differ. Equ.* **2005**, *21*, 586–610. [CrossRef]
6. Hintermüller, M.; Kovtunenko, V.A.; Kunisch, K. A Papkovich–Neuber-based numerical approach to cracks with contact in 3D. *IMA J. Appl. Math.* **2009**, *74*, 325–343. [CrossRef]
7. Barboteu, M.; Bonaldi, F.; Dumont, S.; Mahmoud, C. An energy-consistent discretization of hyper-viscoelastic contact models for soft tissues. *Comput. Meth. Appl. Mech. Eng.* **2024**, *421*, 116785. [CrossRef]
8. Barboteu, M.; Bonaldi, F.; Dumont, S.; Mansour, R. An energy-consistent model of persistent adhesive contact for hyperelastic materials: Theory, discretization, and applications. *Commun. Nonlinear Sci. Numer. Simul.* **2025**, *155*, 109604. [CrossRef]
9. Eberhard, P.; Hüeber, S.; Jiang, Y.; Wohlmuth, B.I. Multilevel numerical algorithms and experiments for contact dynamics. In *Multifield Problems in Solid and Fluid Mechanicsl*; Helmig, R., Mielke, A., Wohlmuth, B.I., Eds.; Springer: Berlin/Heidelberg, Germany, 2006; Volume 28, pp. 271–319. [CrossRef]
10. Chouly, F.; Hild, P.; Renard, Y. *Finite Element Approximation of Contact and Friction in Elasticity*; Birkhäuser: Cham, Switzerland, 2023. [CrossRef]
11. Gustafsson, T.; Stenberg, R. Finite element methods for elastic contact: Penalty and Nitsche. *Raken. Mek.* **2025**, *58*, 46–58. [CrossRef]
12. Jean, M.; Moreau, J.; Raous, M. *Contact Mechanics*; Springer: Berlin/Heidelberg, Germany, 2012. [CrossRef]
13. Amerio, L. Continuous solutions of the problem of a string vibrating against an obstacle. *Ann. Mat. Pura Appl.* **1978**, *59*, 67–96.
14. Kashiwabara, T.; Itou, H. Unique solvability of a crack problem with Signorini-type and Tresca friction conditions in a linearized elastodynamic body. *Phil. Trans. R. Soc. A* **2022**, *380*, 20220225. [CrossRef]
15. Petrov, A. Solvability of a pseudodifferential linear complementarity problem related to a viscoelastodynamic contact model. *Appl. Anal.* **2018**, *97*, 1372–1384. [CrossRef]
16. Fernández-Real, X.; Figalli, A. On the obstacle problem for the 1D wave equation. *Math. Eng.* **2020**, *2*, 584–597. [CrossRef]
17. Kim, J.U. A boundary thin obstacle problem for a wave equation. *Commun. Partial. Differ. Equ.* **1989**, *14*, 1011–1026. [CrossRef]
18. Muñoz-Rivera, J.E.; Portillo-Oquendo, H. Exponential decay for a contact problem with local damping. *Funkcialaj Ekvacioj* **1999**, *42*, 371–388.
19. Schatzman, M.; Bercovier, M. Numerical approximation of a wave equation with unilateral constraints. *Math. Comput.* **1989**, *53*, 55–79. [CrossRef]
20. Akagi, G.; Efendiev, M. Lyapunov stability of non-isolated equilibria for strongly irreversible Allen–Cahn equations. *Proc. R. Soc. Edinb. Sect. A* **2025**, *155*, 1–21. [CrossRef]
21. Carstensen, C.; Gwinner, J. A theory of discretization for nonlinear evolution inequalities applied to parabolic Signorini problems. *Ann. Mat. Pura Appl.* **1999**, *177*, 363–394. [CrossRef]
22. Carvajal, J.J.; Damircheli, D.; Führer, T.; Fuica, F.; Karkulik, M. A space-time finite element method for parabolic obstacle problems. *arXiv* **2025**. arXiv:2503.07808. [CrossRef]
23. Alekseev, G.; Spivak, Y. Optimization-based numerical analysis of three-dimensional magnetic cloaking problems. *Comput. Math. Math. Phys.* **2021**, *61*, 212–225. [CrossRef]
24. Di-Fratta, G.; Pfeiler, C.M.; Praetorius, D.; Ruggeri, M. The mass-lumped midpoint scheme for computational micromagnetics: Newton linearization and application to magnetic skyrmion dynamics. *Comput. Meth. Appl. Math.* **2023**, *23*, 145–175. [CrossRef]
25. Graciani, E.; Mantič, V. Evaluation of the incremental ERR in interface cracks with frictional contact and its application in the coupled criterion of finite fracture mechanics. *Comptes Rendus MÉCanique* **2025**, *353*, 1365–1383. [CrossRef]
26. Sultanova, N. Aggregate subgradient smoothing methods for large scale nonsmooth nonconvex optimisation and applications. *Bull. Aust. Math. Soc.* **2015**, *91*, 523–524. [CrossRef]
27. Ammar-Khodja, F.; Micu, S.; Münch, A. Controllability of a string submitted to unilateral constraint. *Ann. Inst. H. Poincaré (C) Anal. Non Linéaire* **2010**, *27*, 1097–1119. [CrossRef]
28. Casas, E.; Kunisch, K.; Tröltzsch, F. On the value function for optimal control of semilinear parabolic equations. *Nonlinear Anal. Real World Appl.* **2026**, *88*, 104508. [CrossRef]
29. Gou, K.; Mallikarjunaiah, S. Three-dimensional numerical modeling of a stationary v-notch in a porous material constituted by a non-linear response relationship. *Math. Mech. Solids* **2025** . [CrossRef]
30. Rudoy, E.; Itou, H.; Lazarev, N. Asymptotic justification of the models of thin inclusions in an elastic body in the antiplane shear problem. *J. Appl. Ind. Math.* **2021**, *15*, 129–140. [CrossRef]
31. Rudoy, E.M.; Sazhenkov, S.A. The homogenized dynamical model of a thermoelastic composite stitched with reinforcing filaments. *Phil. Trans. R. Soc. A* **2024**, *382*, 20230304. [CrossRef]
32. Anh, N.T.V.; Khan, A.A.; Liu, Z.; Migorski, S. Inverse problems for evolutionary hemi-quasi-variational inequalities with applications. *Set-Valued Var. Anal.* **2025**, *33*, 26. [CrossRef]
33. Burger, M.; Dirks, H.; Frerking, L.; Hauptmann, A.; Helin, T.; Siltanen, S. A variational reconstruction method for undersampled dynamic x-ray tomography based on physical motion models. *Inverse Probl.* **2017**, *33*, 124008. [CrossRef]

34. Jin, B.; Kian, Y.; Zhou, Z. Reconstruction of a space-time-dependent source in subdiffusion models via a perturbation approach. *SIAM J. Math. Anal.* **2021**, *53*, 4445–4473. [CrossRef]
35. Bach, M.; Kovtunenko, V.A.; Khludnev, A.M. Derivatives of the energy functional for 2D-problems with a crack under Signorini and friction conditions. *Math. Meth. Appl. Sci.* **2000**, *23*, 515–534. [CrossRef]
36. Khludnev, A.M.; Kovtunenko, V.A.; Tani, A. Evolution of a crack with kink and non-penetration. *J. Math. Soc. Jpn.* **2008**, *60*, 1219–1253. [CrossRef]
37. Khludnev, A.M.; Sokolowski, J. *Modeling and Control in Solid Mechanics*; Birkhäuser: Basel, Switzerland, 1997. [CrossRef]
38. Zhang, K.; Guo, D.; Lu, K.; Fu, C.; Wang, H.; Dong, C. Reduce the longitudinal and radial vibrations of the autonomous underwater vehicle using the anti-resonance method. *J. Vib. Control* **2025**. [CrossRef]
39. Al-Taweel, A.; Hussain, S.; Mallikarjunaiah, S. Error analysis of an upwind weak Galerkin finite element method for time-dependent hyperbolic problems. *Num. Meth. Partial Differ. Equ.* **2025**, *41*, e70017. [CrossRef]
40. Elguedj, T.; Gravouil, A.; Combescure, A. A mixed augmented Lagrangian-extended finite element method for modelling elastic–plastic fatigue crack growth with unilateral contact. *Int. J. Numer. Meth. Engng.* **2007**, *71*, 1569–1597. [CrossRef]
41. Nikiforov, D.; Stepanov, S.; Lazarev, N. Online meshfree generalized multiscale finite element method for flows in fractured media. *Lobachevskii J. Math.* **2024**, *45*, 5391–5401. [CrossRef]
42. Yoong-Ormaza, C.; Thorin, A.; Legrand, M. The wave finite element method applied to a one-dimensional linear elastodynamic problem with unilateral constraints. In *11th International Conference on Multibody Systems, Nonlinear Dynamics, and Control*; American Society of Mechanical Engineers: Boston, MA, USA, 2015; Volume 6. [CrossRef]
43. Kovtunenko, V.A.; Atlasiuk, O.M. Poroelastic medium with non-penetrating crack driven by hydraulic fracture: FEM approximation using HHT-α and semi-smooth Newton methods. *Algorithms* **2025**, *18*, 579. [CrossRef]
44. Kovtunenko, V.A.; Renard, Y. FEM approximation of dynamic contact problem for fracture under fluid volume control using HHT-$\boldsymbol{\alpha}$ and semi-smooth Newton methods. *Appl. Numer. Math.* **2025**, *218*, 148–158. [CrossRef]
45. Kovtunenko, V.A.; Renard, Y. Convergence analysis of semi-smooth Newton method for mixed FEM approximations of dynamic two-body contact and crack problems. *J. Comput. Appl. Math.* **2026**, *471*, 116722. [CrossRef]
46. Paoli, L.; Schatzman, M. Numerical simulation of the dynamics of an impacting bar. *Comput. Meth. Appl. Mech. Eng.* **2002**, *196*, 2839–2851. [CrossRef]
47. Stoianovici, D.; Hurmuzlu, Y. A critical study of the applicability of rigid-body collision theory. *J. Appl. Mech.* **1996**, *63*, 307–316. [CrossRef]
48. Kovtunenko, V.A. Space-time finite element based primal-dual active set method for the non-smooth problem of impact of rigid obstacle by elastic bar. *Comput. Math. Model.* **2025**, *36*, 571–596. [CrossRef]
49. Kovtunenko, V.A. Space-time primal-dual active set method: Benchmark for collision of elastic bar with discontinuous velocity. *Computation* **2025**, *13*, 210. [CrossRef]
50. Kovtunenko, V.A.; Petrov, A.; Renard, Y. Space-time FEM solution of dynamic contact problem with discontinuous velocity for multiple impact of deformed bar using PDAS method. *Math. Meth. Appl. Sci.* **2025** . [CrossRef]
51. Chouly, F.; Renard, Y. Explicit Verlet time-integration for a Nitsche-based approximation of elastodynamic contact problems. *Adv. Model. Simul. Eng. Sci.* **2018**, *5*, 31. [CrossRef]
52. Khenous, H.B.; Laborde, P.; Renard, Y. Comparison of two approaches for the discretization of elastodynamic contact problems. *Comptes Rendus Math.* **2006**, *342*, 791–796. [CrossRef]
53. Aimi, A.; Cattivelli, S.; Chouly, F.; Guardasoni, C. Nitsche's Energetic BEM-FEM Coupling for Wave Propagation in 2D Multidomains. 2025. Available online: https://www.researchgate.net/publication/399190480_Nitsche's_energetic_BEM-FEM_coupling_for_wave_propagation_in_2D_multidomains (accessed on 13 January 2026).